Non-propagating Form Drag and Turbulence Due to Stratified Flow over Large-scale Abyssal Hill Topography

Jody M. Klymak, Jody Klymak, University of Victoria, Victoria, BC, Canada

*

ABSTRACT

Drag and turbulence in steady stratified flows over "abyssal hills" have been parameterized using linear theory and estimated rates of energy cascade due to wave-wave interactions. This theory has no drag or energy loss due to large-scale bathymetry because waves with intrinsic frequency less than the Coriolis frequency are evanescent. Previous numerical work has tested the theory by high-passing the topography and estimating the resulting turbulence. Here we show that the large-scale evanescent part of the internal wavefield is actually non-linear and turbulent, and that the dissipation is approximately twice that of the waves generated by the small-scale bathymetry. Simulations containing both small- and large-scale bathymetry have more dissipation than just adding the large- and small-scale dissipations together, so the scales couple. The large-scale turbulence is localized, generally in the lee of large obstacles, presenting an important real-world sampling problem. Medium-scale regional or global models partially resolve the "non-propagating" wavenumbers, leading to the question of whether they need the large-scale energy loss to be parameterized. Varying the resolution of the simulations indicates that if the ratio of grid cell height to width is less than the root-mean-square of the topographic slope, then the dissipation is over-estimated in coarse models (by up to 25%); conversely it can be greatly underestimated (by up to a factor of two) if the ratio is greater than the root-mean-square slope. Most regional simulations are likely in the second regime, and should have extra drag added to represent the large-scale bathymetry, and the deficit is at least as large as that parameterized for "abyssal hills".

1. Introduction

Slowly varying stratified flow over topography occurs throughout the ocean either due to mean flows or eddies. By creating internal waves that have to break in the water column, mean flow over rough topography is one of the possible pathways by which the interior of the ocean is mixed, with long-term consequences for overturning circulations and distribution of tracers in the ocean.

The linear theory for steady stratified flow over topography is due to Bell (1975), who derived how to calculate the rate energy is removed from the mean flow over a topography composed of a broad range of spectral components. Rate of energy lost implies a form drag over the topography of $F = U_0 D$, where F is the radiated energy, D is the form drag and U_0 the mean flow speed. Here we will generally deal with F, but it is directly proportional to the drag. Tests with two-dimensional topography indicate that Bell's theory is relevant for oceanic scales (Nikurashin and Ferrari 2010), though corrections need to be made if the topography varies in the cross-flow direction (Nikurashin et al. 2014), with substantially less generation of internal waves for large topography (Nh/U_0 large, where is h the root-mean-squared topographic height and N the buoyancy frequency. This is called the "steepness parameter" by Nikurashin et al. (2014), we will call the "inverse Froude number"). However, freely propagating internal waves are only generated for topographic wavenumbers $k > f/U_0$, where f is the Coriolis frequency. For larger scale topography the response is evanescent, with a vertical decay scale given by $\left(f^2 - U_0^2 k^2\right)^{1/2} / Nk$. For large wavelengths, this decay scale can reach hundreds of meters. In their work comparing to theory, (Nikurashin et al. 2014) bandpassed the bathymetry so that $f/U_0 < k < N/U_0$. The extra mixing and drag due to these "abyssal hills" is believed to be significant to accurate global numerical simulations (i.e. Trossman et al. 2016), and in calculations of overturning circulations (i.e. de Lavergne et al. 2016).

This leads to the central question of this paper: how important is the large-wavenumber topography to the drag and turbulence on the mean flow? In order to apply Bell's theory the inverse Froude number, Nh/U_0 needs to be small. For a flow over bandpassed topography, this is close to being met for abyssal oceanic scales, where typical values used by (Nikurashin et al. 2014) were $N = 10^{-3}$ rad s^{-1}, $h = 80$ m, and $U_0 = 0.1$ m s^{-1}, so $Nh/U_0 \approx 0.8$. However, the full bathymetric spectrum that they bandpassed from (and we use below) has a root-mean-squared height of $h = 305$ m, so a characteristic $Nh/U_0 \approx 3$. This means that the large-scale part of the red topographic spectrum is non-linear and not amenable to linear treatment (Bell 1975). Rather, upstream blocking and downstream hydraulic effects are predicted to be important (Baines 1995; Klymak et al. 2010), as well as an increased tendency for the flow to go around obstacles in the cross-flow (Nikurashin et al. 2014).

Here we report a number of simulations based on those by Nikurashin et al. (2014). As described in section 2, simulations are made over three types of bathymetry from the same spectrum used by Nikurashin et al. (2014), one where the topography has been BANDPASSED, as they present, one where the topography has been LOWPASSED at the same low wavenumber used in the bandpass, and a third where the FULL bathymetric spectrum is used (small-cap typography indicates the bathymetry in what follows). Because we need to resolve the large scales, these model runs are carried out on a very large domain. The results for simulations over these topographies at four different mean flow speeds are presented (section 3), showing that the large-scale LOWPASSED topography has approximately twice the dissipation of the small-scale (BANDPASS), and all the bathymetry scales together (FULL) have somewhat more than the sum of the two simulations across the velocities investigated. The implications for sampling are briefly discussed (section 4) due to the localized nature of the turbulence generated by the large-scale topography. We also investigate whether the turbulence and drag from the large-scale topography will be represented in regional- and global-scale ocean models.

2. Model configuration

Here we use a similar model machinery to (Nikurashin et al. 2014), wherein we assume a doubly periodic domain with constant stratification and a mean flow in the x-direction forced over rough topography. The strength of the flow maintained by a body force meant to simulate an externally imposed surface pressure gradient. Because the full-resolution $\Delta x = \Delta y = 100$ m model is expensive, we spin the model up using a coarse-resolution model over the same domain with $\Delta x = \Delta y \approx 1000$ m. The runs were carried out over a doubly periodic lateral domain of 409.6 km in x, and 118.4 km in the y direction. Total simulation depth was 4000 m, with $\Delta z = 10$ m at all depths. We needed a large lateral domain in order to capture enough variance in the large-scale topography.

a. Stratification, forcing, and spinup

The model is run with a constant initial stratification of $N = 10^{-3}$ s^{-1}. An initial uniform velocity was set in the x-direction ($U_0 = 0.02, 0.05, 0.1, 0.15$ ms^{-1}), and momentum was maintained in the flow using a universal body force in the y-direction: $F_B = +fU_0$. We chose $f = +10^{-4}$ rad s^{-1}.

Coarse 1-km runs were spun up for 200 h. These runs had weak relaxation to the background stratification in a region that covered 25% of the domain in the y-direction, and the whole domain in the x-direction. The fine-resolution runs had no buoyancy relaxation. There was a loss of stratification near the topography in the simulations (FIG. 1b), which is unavoidable given the 410-km along-flow domain length (47-d transit time at 0.1 m s^{-1}) without resorting to a-physical forcing in the interior of the domain of interest.

b. Bathymetry

The basic bathymetry used for the simulations is a stochastic version of the bathymetric spectrum used in Nikurashin et al. (2014), given by:

$$P_{2D}(k,l) = \frac{2\pi H^2(\mu-2)}{k_0 l_0}\left(1+\frac{k^2}{k_0^2}+\frac{l^2}{l_0^2}\right)^{-\mu/2} \quad (1)$$

where $H = 305$ m is the root-mean-square of the topographic height, $\mu = 3.5$ is a fit parameter setting the high-wavenumber slope, and $k_0 = l_0 = 1.8\times10^{-4}$ rad m^{-1} are fit parameters that set the wavelength at which the spectrum of the topography starts to flatten out (FIG. 2, gray dashed spectrum).

Three variations on this topography are used. The FULL topography contains variance at all wavenumbers (FIG. 2, red line), bounded at the large scale by the domain size, and at the small scales by the grid resolution. The BANDPASS topography (FIG. 2, blue line) is composed of wavenumbers $f/U_0 < |\mathbf{k}| < N/U_0$, and the LOWPASS topography of wavenumbers $|\mathbf{k}| < U_0/f$, which corresponds to a wavelength of 6 km.

The qualitative effect on the flow of the low-wavenumber topography is clear from an example cross-section (FIG. 1a). There are peaks and valleys such that the FULL topography spans 1250 m of water depth. The scale of this topography strongly affects the inverse topographic Froude number Nh/U, which is approximately 0.8 for the BANDPASS topography, but greater than 3 for the FULL topography. The goal of this paper is to determine the effect this large-scale topography has on the turbulence.

c. Resolution

All models had vertical resolution of 10 m over 4000 m depth. For numerical efficiency, the models were run for 200 h of spinup at approximately 1-km horizontal resolution over a 409.60

km by 118.40 km domain (`nx = 416`, and `ny = 128`). These coarse runs were then interpolated laterally onto (exactly) 100-m horizontal resolution models and run for another 20 h. There were a few valleys where extrapolation was necessary, so the flow was set to the background flow speed, and the density to the background density profile in these regions. The time scales work well because it is the large-scale near-inertial internal waves that are slow to propagate in the vertical, whereas the smaller-scale waves setup quite rapidly. We diagnose the rate of change of energy in the energy budgets below, and the residual is small.

d. Model configuration

The `MITgcm` was used for all simulations (Marshall et al. 1997), in a manner analogous to previous work at similar scales (Buijsman et al. 2014; Klymak et al. 2016). Background explicit vertical and horizontal viscosity and diffusivity are kept low ($K_\rho = \nu = 10^{-5}$ m^2 s^{-1}) except in the presence of resolved density overturns where the vertical viscosity and diffusions are increased in a manner consistent with the expected Thorpe scale (Klymak and Legg 2010). There is also numerical diffusivity and dissipation due to the second-order flux-limiting temperature advection scheme (`tempAdvScheme=77`; see the MITgcm manual). For the work carried out here, the terms in the energy budget are all calculated and the residual is identified as the dissipation. However, the spatial distribution of explicit dissipation (calculated from the explicit viscosities and local shears) is similar to the inverse energy budgets. The model is run in hydrostatic mode for these simulations.

3. Results

a. Overview of simulated flows

Example slices from the simulations illustrate the differences between the bathymetries (FIG. 3 and FIG. 4). The BANDPASS bathymetry simulations yield a bottom-intensified (almost) steady internal wave field that has radiated energy through the domain (FIG. 3c). Directly near the sea floor there is evidence of enhanced numerical dissipation due to the flux-limiting advection scheme (FIG. 4c) as evinced by the pixelation of the velocity field at these depths.[1]

The flow over the FULL and LOWPASS bathymetry shows the impact of including the large-scale bathymetry (FIG. 3a,b). First, there are approximately 100-km-scale regions of barotropic acceleration and deceleration due to the inhomogeneous nature of the bottom form drag. Further, there are thick regions of acceleration and deceleration near the topography of the same order as the strength of the forcing. These regions scale in thickness roughly as $\Delta = \pi U_0/N \approx 300$m for the flows here (see below where we change U_0) and represent the thickness of the active layer of the flow near the bathymetry (i.e. Klymak et al. 2010). These regions are the same order as the bathymetric scale, so the flow is substantially non-linear, with blocking, steering, and hydraulic responses all expected phenomena.

Also of note is the existence of radiating internal waves in LOWPASS solutions, despite there being no topographic variance for wavenumbers $k > N/U_0$ (FIG. 4b). These waves have relatively high amplitudes, and are because the local flow over the bathymetry is faster than the mean flow, making $f/U < f/U_0$; note that the clearest examples of wavepackets are seen in regions of enhanced near-bottom velocities (FIG. 3b).

The flows over the large-scale topography have variance out to low wavenumbers, as confirmed by looking at lateral temperature spectra above the topography (FIG. 5). The BANDPASS run, as expected, has variance that is largely confined in the freely propagating regime. This energy drops, particularly for large scales, with distance from the topography (FIG. 5b). For the runs with large-

[1] We could remove these numerical artifacts by increasing our explicit viscosity, but at the expense of decreasing our simulated Reynolds number away from the topography. The conceit used in this paper is that the numerical dissipation occurs in highly non-linear regions anyway, and reflects a cascade to turbulence.

scale topography, there is substantial variance at large scales (FIG. 5a, red and purple lines). By 2300 m depth, this variance also drops, and drops selectively at the smaller scales. While there is undoubtably some non-linearity in this response, it is consistent with Bell's solutions that predict an exponential decay of the linear response with height above the topography proportional to the horizontal wavenumber, k.

b. Laterally averaged energy budgets

We form an energy budget of the simulated flows that we then integrate laterally (and then vertically) to determine the important terms, and take a residual to get the dissipation in the model. We linearize the potential energy term, which given the relatively small vertical displacements is an acceptable approximation, and use a Boussinesq approximation, so that

$$E = \frac{1}{2}\mathbf{u}^2 + \frac{1}{2}\frac{g}{N_b^2}\left(\frac{\rho'}{\rho_0}\right)^2 \tag{2}$$

where $\mathbf{u}$ is the velocity vector, g the acceleration due to gravity, $N_b^2 = -\frac{g}{\rho_0}\frac{\mathrm{d}\rho_b}{\mathrm{d}z}$ is the square of the background buoyancy frequency, $\rho' = \rho(x,y,z,t) - \rho_b(z)$ is the density anomaly relative to the background density profile $\rho_b(z)$, and $\rho_0 = 1000\ \mathrm{kg\,m^{-3}}$ is the reference density.

The background density profile $\rho_b(z)$ is calculated from the modeled density field following Tseng and Ferziger (2001). Akin to the sorting procedure proposed by Winters et al. (1995), the cumulative distribution of water area as a function of density is calculated and matched to the cumulative distribution of water area as a function of depth. Interpolating from one distribution to the other gives the depth of each density in the distribution, and mapping back to depth gives a profile of density that is sorted by depth[2]. The background density gradient changes (slightly) in the hour of simulation that we form our energy budget over, allowing us to calculate the change in

[2]the computational advantage is that a histogram is far easier to form than sorting and re-distributing the fluid, particularly in a convoluted geometry, though the grid cells all must be the same size

background potential energy in the model (E_B) between model snapshots as:

$$E_B = \frac{1}{V}\int_{-H}^{0} A(z)\,\rho_b\, g z\,\mathrm{d}z \tag{3}$$

where V is the total volume of water.

The horizontally averaged energy budget is then:

$$\frac{\mathrm{d}\overline{E}}{\mathrm{d}t} = -\frac{\mathrm{d}}{\mathrm{d}z}\overline{wp} - \frac{\mathrm{d}}{\mathrm{d}z}\overline{wE} + fU_0\overline{v} - D \tag{4}$$

where w is the vertical velocity, $p = \frac{P-P_0}{\rho_0}$ the pressure anomaly compared to a reference pressure profile $P_0(z) = -\int_z^0 \rho_0 g\,\mathrm{d}z$, $fU_0\overline{v}$ is the energy input via the body force, and D is the residual due to dissipation and changes in the background potential energy (E_b). The first two terms on the right-hand side each integrate to zero in the vertical, but serve to redistribute energy vertically in the water column. The divergence of the nonlinear vertical advection of energy is non-zero, and largely in opposition to the wave pressure work divergence. The net effect is that the dissipation is inferred to occur slightly above where the energy is put into the system by the body force. For readers that prefer a form-drag formulation, note that in this system the imposed body force can be shown to be identically equal to the work done by the form-drag on the flow.

1) Energy changes with topography

The vertical integral of the energy budgets show that the simulations are not perfectly in steady state, with the rate of change term (FIG. 6, red line) varying between 5% and 30% of the body force term (FIG. 6, purple line). We consider this an uncertainty in the energy budget - if allowed to run to full steady state, it is possible that the dissipation would increase, or that the rate of conversion (as represented by the body force) would go down. So below, we use this to assign an uncertainty to the dissipation estimate, putting the "dissipation" between the body force and the residual.

The vertical integral of the energy budget shows the clear difference between the simulations over the different topography types. The BANDPASS simulation has the least amount of energy loss from the mean flow of 11.7 ± 0.3 mW m^{-2} (FIG. 6c) concentrated near the seafloor in a thin layer approximately 300 m thick This corresponds very well with the 10 mW m^{-2} of energy conversion found by Nikurashin et al. (2014) for similar parameters. However, when just the LOWPASS bathymetry is used, there is substantially more dissipation (21.0 ± 4.0 mW m^{-2}) than the BANDPASS simulation. This is because the flow is blocked or accelerated in regions dues to the large-scale topography.

The FULL topographic simulation has more dissipation than the other two simulations combined (39.5 ± 0.8 mW m^{-2}, FIG. 6a). Dissipation extends higher into the water column than the BANDPASS simulation, partially because the topography extends higher, but also because turbulent features are on the order $\pi U/N_0 \approx 300$ m high (FIG. 4a). Overall, the high dissipation covers about 800 m of depth. (Note that we have not presented dissipation versus height off bottom, which is not possible to do with the residual budgets we are making here).

The background potential energy changes significantly in these simulations, with a total between 15% and 40% of the energy budget residual. These simulations are not direct numerical simulations, so the exact ratio of dissipation to irreversible buoyancy flux should not be taken very seriously. However, it does indicate that vertical mixing can be substantial in these flows as indicated by the erosion of the near-bottom stratification (FIG. 1b).

2) ENERGY CHANGES WITH MEAN FLOW SPEED

The same model set up was used to simulate flows with mean flows of $U_0 = 0.02$, 0.05, 0.10, and 0.15 m s^{-1}. Note that the three types of topography were *not* changed in these runs, so the BANDPASS topography, bandpassed between 600 m and 6 km scales, would not exactly match the lower and upper bounds of the permissible internal waveband set by $f/U_0 < k < N/U_0$. With this in mind, it is clear that stronger forcing leads to stronger dissipations with all three topographies (FIG. 7). As with $U_0 = 0.10\ \mathrm{m\,s^{-1}}$, the BANDPASS topography has significantly less dissipation than the LOWPASS and FULL topography, by about a factor of 2 and 3 respectively. These differences drop as higher mean flow speeds are simulated because the BANDPASS simulations have a steeper power law with U_0 than the other two topographies.

The power law of the dissipation versus U_0 in the BANDPASS simulations of 1.95 is very close to the theoretically expected value of 2 (FIG. 7, light blue). The power laws for the LOWPASS and FULL simulations are less than this value, with the LOWPASS power law being 1.7 and the FULL power law slightly steeper at 1.76 (FIG. 7, purple and red respectively). For the LOWPASS case, a likely reason for the lower power law is that as U_0 increases, the amount of blocking, and hence the strength of downstream hydraulic jumps decreases as Nh/U_0 decreases. Hence the flow becomes more linear, and the non-linearity that drives the non-propagating drag decreases. The regime in these runs is $Nh/U_0 \approx 25, 10, 5$ and 3, so we are between the classical "linear" wave drag regime and the strongly non-linear wave drag regime.

The dissipation in the FULL simulation exceeds the sum of the LOWPASS and BANDPASS dissipations, so the different wavenumbers in the topography obviously interact. The simplest explanation of this is that the large-scale elements in the FULL simulation locally accelerate or decelerate the flow over the small-scale elements. While the corresponding mean is close to U_0, the mean of $\left\langle U^2 \right\rangle > U_0^2$ so the dissipation due to the small-scale topography is greater than in the BANDPASS case. We can see evidence for this in the snapshots (FIG. 3a) where there appears to be more internal wave activity emanating from regions where the flow has been accelerated versus regions where it has been decelerated (recall that the velocity anomaly is plotted, so deep blue colors are getting close to zero velocity, not negative velocity).

4. Summary and Discussion

Simulations of mean flow over topography that include large scales exhibit significant energy removal from the mean flow (and hence form drag) over and above that exerted by steady flow over the smaller scales. This is despite the fact that flow over the large scales cannot emit propagating internal waves because the topographic wavenumbers $k < f/U_0$. In steady state, this non-propagating part of the wavefield would not extract energy from the mean flow under linear dynamics because the disturbances would be evanescent. However, at the large scales $Nh/U_0 > 1$, and the flow is significantly non-linear and dissipative, with flow blocking upstream of topography, and breaking waves downstream. This means that at the parameter ranges considered here the dissipation due to the full-spectrum topography flows is more than 3 times as much as just the flow over high wavenumbers, a result that holds across a broad range of velocities over the same topography.

a. Scaling energy loss from mean flow

It would be desirable to predict the dissipation due to the large-scale topography. Due to the non-linearity and three dimensionality, this does not appear simple to do, and certainly there is no linear theory to appeal to like that used for the high-wavenumber flows. A rough estimate for large-Nh/U_0 flows can be derived from the isolated topography case (Klymak et al. 2010), where the form-drag integrated along an obstacle can be approximated by:

$$F_d = \rho_0 N U_0 h_m^2 \frac{\pi}{2}\left(1 + \pi \frac{U_0}{Nh_m} - 2\pi^2 \left(\frac{U_0}{Nh_m}\right)^2\right) \tag{5}$$

Here, a reasonable value for an obstacle height is $h_m = 350 - 500$ m. Turning this into an energy density requires assuming a spacing between obstacle peaks, which is approximately $\Delta x \approx 100$ km (FIG. 1a). This rough calculation yields a dissipation of $17 - 33\ \mathrm{mW\,m^{-2}}$ for $U_0 = 0.1\ \mathrm{m\,s^{-1}}$, which brackets the $23\,\mathrm{mW\,m^{-2}}$ simulated for the LOWPASS topography simulation. The power law of this parameterization scales as U_0^2 for large Nh/U_0, but as Nh/U_0 gets smaller the correction terms start to dominate, flattening the power law, as observed as U_0 was increased (FIG. 7). Of course the assumptions that go into equation (5) are not valid at lower Nh/U_0, so the analogy breaks down. Future effort should be aimed at parameterizing the large-scale drag and/or dissipation using a-priori calculations.

b. Lateral inhomogeneity

The reason we had to use such a large modeling domain is that the dissipation caused by the large-scale topography is spatially inhomogeneous (FIG. 8). Sensitivity tests on the 1-km coarse models indicated that dissipation results converged as the domain approached 100-km by 400-km, so that was what was used for the simulations above. The reason for that can be readily seen (FIG. 8a), where the regions of strong dissipation are on the scale of 50-100 km in the along-flow direction, and about 25 km in the cross-flow direction. Subsets of these regions have a strong potential to be biased.

The distribution of the dissipation has important implications for oceanographic sampling. If an experiment were deployed similar to DIMES (St. Laurent et al. 2012) where on the order of 34 vertical profiles could be accomplished, then the mean dissipation rate could be substantially biased as shown by a Monte Carlo sampling of the sample means (FIG. 8b, blue line). The median of this distribution is 0.6 the mean of the dissipation in the simulation, so the expected bias is relatively large and biased low, but there is a significant fraction of the Monte-Carlo means that are many times the actual mean. The problem is worse if the sampling is deterministic, or biased towards sampling hot spots, and of course a few individual moorings could be placed anywhere in this region and get answers that are either far too low, or far too high (i.e. Waterman et al. 2013; Brearley et al. 2013).

c. Resolution dependence: do coarser models have the dissipation?

The argument for including a parameterization for drag and mixing due to "abbysal hills" is that numerical models cannot simulate these scales, and hence the extra drag and mixing should be added. In this paper, we argue that the drag and dissipation due to the large-scale (stochastic) topography is significantly larger. However, it is entirely possible that coarse models already simulate the turbulence and drag due to this large-scale part of the topographic spectrum because they are (partially) resolving them well-enough.

We ran the same simulations over a range of lateral resolutions (1.0, 2.5, and 4.0 km) and vertical resolutions (between 10 m and 307 m). We used the LOWPASS bathymetry, so there is no topographic roughness at scales smaller than 6 km. We used the same nominal forcing noted above with flow speeds of $U_0 = 0.1\ \mathrm{m\,s^{-1}}$. Lateral and vertical model resolution strongly affect the resulting dissipation, and interestingly, the two effects counter each other (FIG. 9). For a very high lateral resolution by global-model standards (1 km) the agreement with the 100-m resolution runs drops as vertical resolution is coarsened, with the energy loss plateauing relatively quickly at about 0.6 of the loss in the high-resolution run. To compare with the energy budgets above, this is 15 $\mathrm{kW\,m^{-1}}$. If the model has a well-parameterized "abyssal hill" dissipation (i.e. BANDPASS) of 12 $\mathrm{kW\,m^{-1}}$, then the total dissipation inferred in this coarse model is 27 $\mathrm{kW\,m^{-1}}$, compared to 40 $\mathrm{kW\,m^{-1}}$, or 67%. This is not terrible disagreement, and the use of the "abyssal hill" parameterization will definitely help get the correct dissipation and drag.

For coarser simulations, $\Delta x = 4$ km, the energy loss is exaggerated at fine vertical resolutions (FIG. 9, blue line), and then suddenly drops to much less than the fine-resolution runs for $\Delta z >$

200 m. This occurs as $\Delta z/\Delta x > \left\langle (dh/dx)^2 \right\rangle^{1/2}$ the root-mean-square of the topographic slope (vertical colored lines in both plots). Therefore, the guidance for numerical modelers running at regional-scale resolutions is somewhat ambiguous. If models resolve the root-mean-squared of the topographic slope (approximately $2\pi/k_0$, where k_0 is the topographic bandwidth parameter described above), then they will slightly over-predict mean-flow stratified drag. If the vertical resolution is too coarse, then they will not resolve this drag, and they will need to increase their drag significantly more than that just due to the parameterizations for "abyssal hills".

d. Concluding Remarks

In conclusion, in the linear limit large-wavenumber topography should not generate radiating internal waves, and hence should not have drag or play a part in the energy budget. However, such topography is actually the dominant term in the energy budget because of non-linearity and turbulence in an ocean-relevant regime. Coarse-scale models are challenged to get this large-scale "non-propagating" drag right, though exactly whether they over- or under-predict the drag depends on the ratio of vertical to horizontal resolution. Finally, the dissipation due to the large-scale bathymetry is very spatially inhomogeneous, leading to a strong observational challenge. Further studies are planned to try to predict the low-wavenumber drag over the stochastic topography better, and to incorporate it into numerical models so that drag is not "double counted".

Acknowledgments. Thanks to Raffaele Ferrari, Brian Arbic, and Kurt Polzin for helpful discussions on this manuscript, particularly Kurt Polzin for introducing the term "non-propagating wave drag". This work was funded under the Office of Naval Research Flow Encountering Abrupt Topography Defence Research Initiative (grant N00014-15-1-2585), and NSERC Discovery Grant 327920-2006. Thanks to Odessa Murray who manages the High Performance

Computing accounts for ONR. Example model setup and processing scripts are available at `http://web.uvic.ca/~jklymak/leewaves17`.

References

Baines, P. G., 1995: *Topographic Effects in Stratified Flows*. Cambridge Univ. Press, New York.

Bell, T. H., 1975: Topographically generated internal waves in the open ocean. *J. Geophys. Res.*, **80**, 320–327.

Brearley, J. A., K. L. Sheen, A. C. Naveira Garabato, D. A. Smeed, and S. Waterman, 2013: Eddy-induced modulation of turbulent dissipation over rough topography in the southern ocean. *J. Phys. Oceanogr.*, **43**, doi:10.1175/jpo-d-12-0222.1, 2288–2308.

Buijsman, M. C., J. M. Klymak, S. Legg, M. H. Alford, D. Farmer, J. A. MacKinnon, J. D. Nash, J.-H. Park, A. Pickering, and H. Simmons, 2014: Three-dimensional double-ridge internal tide resonance in Luzon Strait. *J. Phys. Oceanogr.*, **44**, doi:10.1175/JPO-D-13-024.1, 850–869.

de Lavergne, C., G. Madec, J. Le Sommer, A. J. G. Nurser, and A. C. Naveira Garabato, 2016: On the consumption of antarctic bottom water in the abyssal ocean. *J. Phys. Oceanogr.*, **46**, doi:10.1175/jpo-d-14-0201.1, 635–661.
`http://dx.doi.org/10.1175/JPO-D-14-0201.1`

Klymak, J. M., S. Legg, and R. Pinkel, 2010: High-mode stationary waves in stratified flow over large obstacles. *J. Fluid Mech.*, **644**, doi:10.1017/S0022112009992503, 312–336.

Klymak, J. M., and S. M. Legg, 2010: A simple mixing scheme for models that resolve breaking internal waves. *Ocean Modell.*, **33**, doi:10.1016/j.ocemod.2010.02.005, 224 – 234.

Klymak, J. M., H. L. Simmons, D. Braznikov, S. Kelly, J. A. MacKinnon, M. H. Alford, R. Pinkel, and J. D. Nash, 2016: Reflection of linear internal tides from realistic topography: The Tasman continental slope. *J. Phys. Oceanogr.*, doi:10.1175/jpo-d-16-0061.1.

Marshall, J., A. Adcroft, C. Hill, L. Perelman, and C. Heisey, 1997: A finite-volume, incompressible Navier-Stokes model for studies of the ocean on parallel computers. *J. Geophys. Res.*, **102**, doi:10.1029/96JC02775, 5753–5766.

Nikurashin, M., and R. Ferrari, 2010: Radiation and dissipation of internal waves generated by geostrophic motions impinging on small-scale topography: Theory. *Journal of Physical Oceanography*, **40**, 1055–1074.

Nikurashin, M., R. Ferrari, N. Grisouard, and K. Polzin, 2014: The impact of finite-amplitude bottom topography on internal wave generation in the southern ocean. *J. Phys. Oceanogr.*, **44**, doi:10.1175/JPO-D-13-0201.1, 2938–2950.

St. Laurent, L., A. Naveira Garabato, J. Ledwell, A. Thurnherr, J. Toole, and A. Watson, 2012: Turbulence and diapycnal mixing in Drake Passage. *Journal of Physical Oceanography*, **42**, 2143–2152.

Trossman, D. S., B. K. Arbic, J. G. Richman, S. T. Garner, S. R. Jayne, and A. J. Wallcraft, 2016: Impact of topographic internal lee wave drag on an eddying global ocean model. *Ocean Modell.*, **97**, doi:10.1016/j.ocemod.2015.10.013, 109–128.

Tseng, Y.-h., and J. H. Ferziger, 2001: Mixing and available potential energy in stratified flows. *Physics of Fluids*, **13**, doi:10.1063/1.1358307, 1281–1293.

Waterman, S., A. C. Naveira Garabato, and K. L. Polzin, 2013: Internal waves and turbulence in the Antarctic Circumpolar Current. *J. Phys. Oceanogr.*, **43**.

Winters, K. B., P. N. Lombard, J. J. Riley, and E. A. D'Asaro, 1995: Available potential energy and mixing in density-stratified fluids. *J. Fluid Mech.*, **289**, 115–128.

LIST OF FIGURES

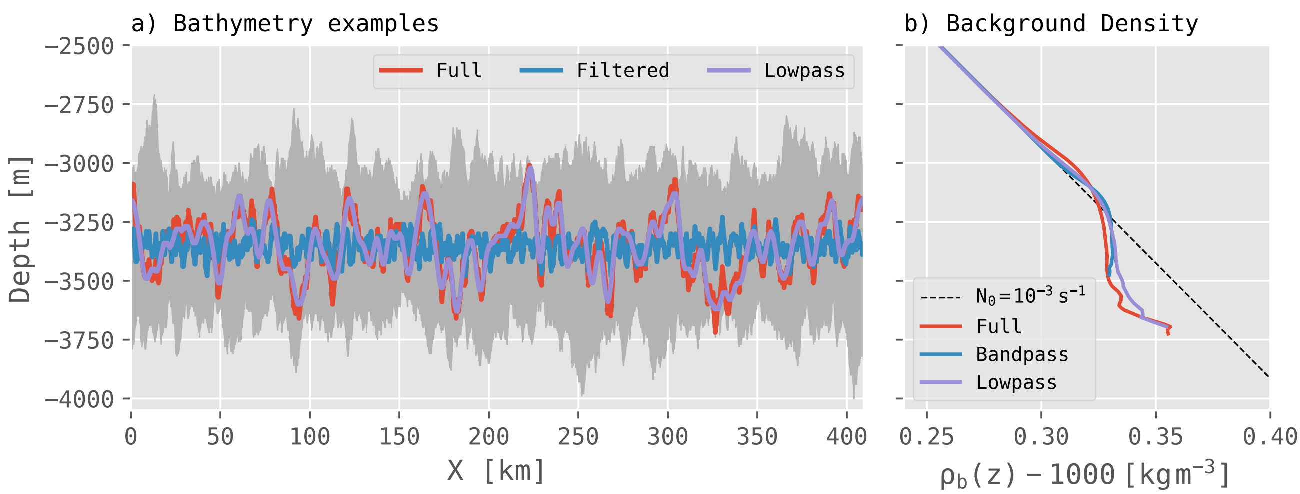

FIG. 1. a) Cross sections of topography used at $y = 50$ km. The gray shading indicates the maximum and minimum of the FULL topography across the whole domain. b) Background density profiles for the flow over the three topographies at 220 h into the simulation. The nominal stratification of $N_0 = 10^{-3}$ s^{-1} is indicated with the solid dashed line and most of the water column above $z = -2750$ m follows this curve during the simulation, except for some water at the very top that has some modification (not shown). Near-bottom modification is substantial, though mostly in a 350-m deep layer.

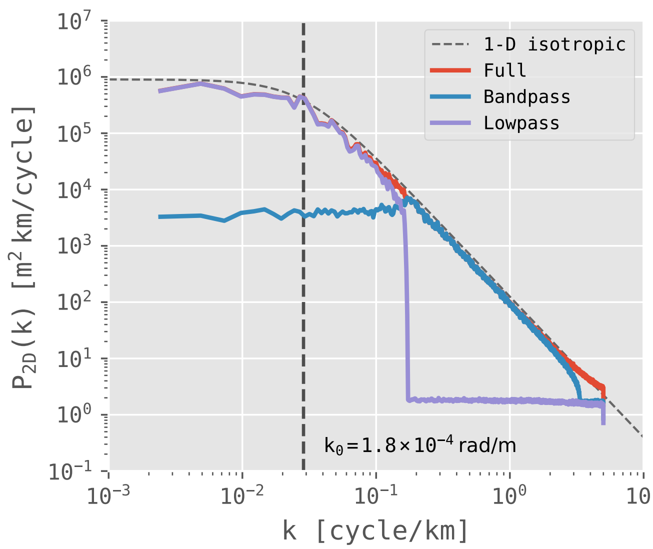

FIG. 2. Spectra of topography used. The 1-D isotropic spectrum (gray dash) is the 1-dimensional version of the 2-D spectrum used to generate the bathymetry used in the paper. The FULL bathymetry has bathymetric variability at all the wavenumbers. The topography that make up the BANDPASS spectrum (blue) has been bandpassed with $2\pi/6$ km $< |\mathbf{k}| < 2\pi/0.6$ km, following (Nikurashin et al. 2014). The LOWPASS spectrum (purple) has been low-passed, removing variance for wavenumbers $|\mathbf{k}| > 2\pi/6$ km. The low-wavenumber roll-off, k_0, is indicated with the vertical dashed line.

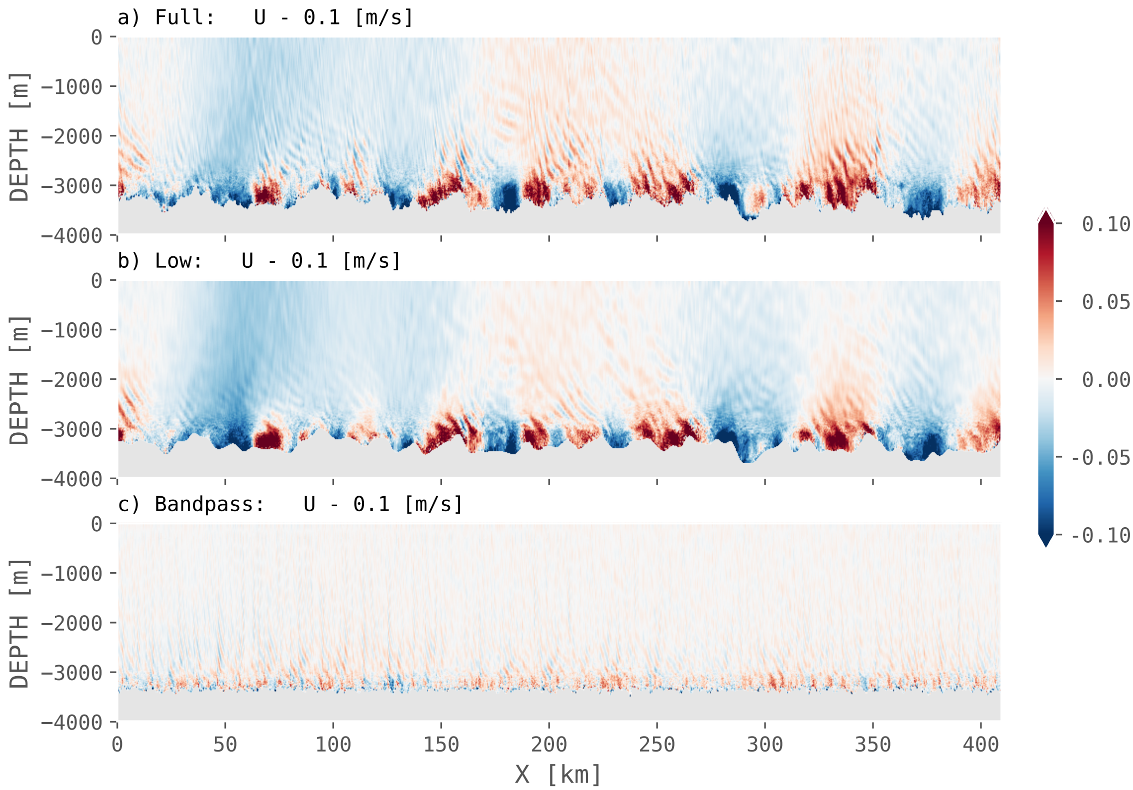

443 FIG. 3. Snapshots at y=50 km of along-flow velocity anomaly ($U - U_0$, where $U_0 = 0.1$ m s^{-1}) for a) the
444 FULL bathymetry, b) the LOWPASS bathymetry, and c) the BANDPASS bathymetry.

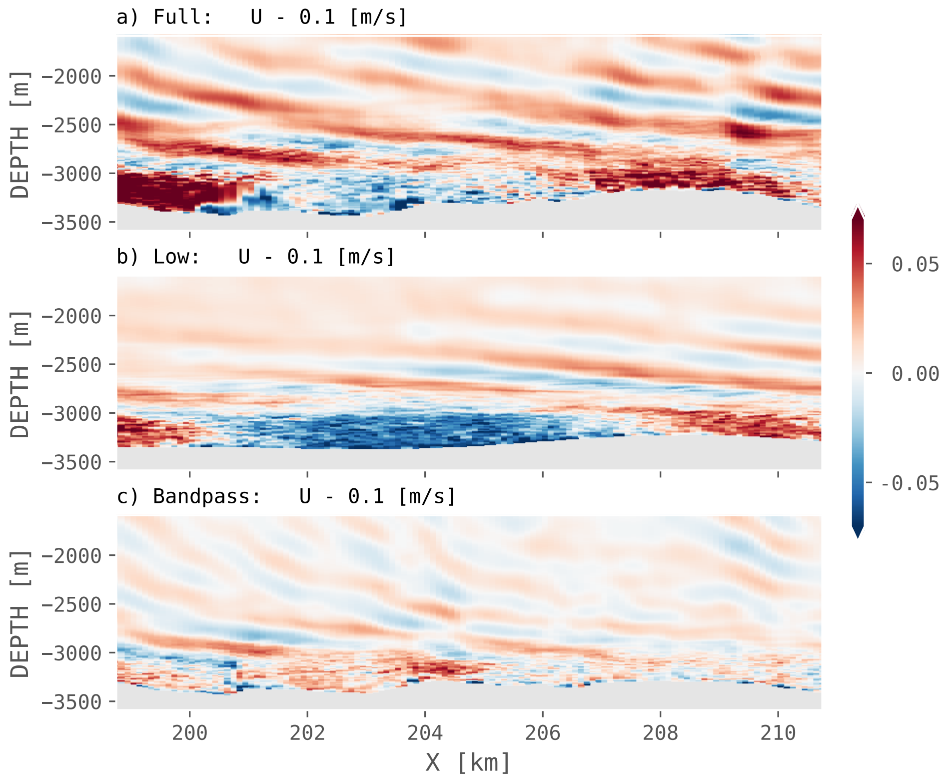

FIG. 4. Snapshots at y=50 km of along-channel velocity anomaly ($U - U_0$, where $U_0 = 0.1\ \mathrm{m\,s^{-1}}$) zoomed into a 12-km wide region at the center of the domain, for a) the FULL bathymetry, b) the LOWPASS bathymetry, and c) the BANDPASS bathymetry.

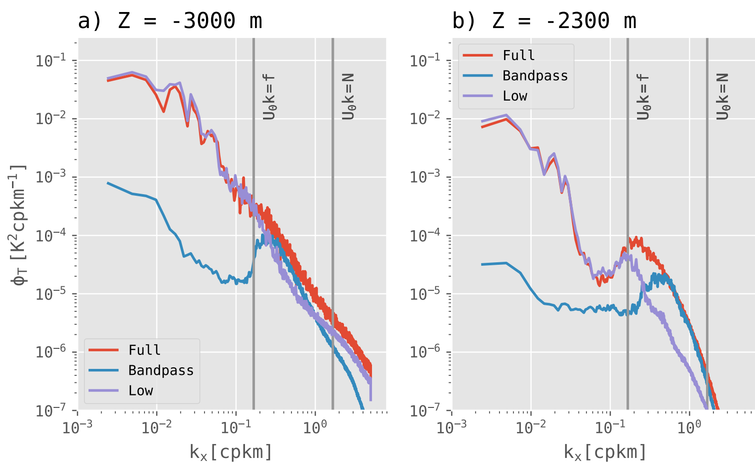

448 FIG. 5. Lateral temperature spectra at a) 3000 m and b) 2300 m depth for the three topographies ($U_0 =$

449 $0.1\ \mathrm{m\,s^{-1}}$), averaged across the domain in the y-direction. The vertical grey lines demark the region of freely

450 propagating internal waves $f < U_0 k < N$.

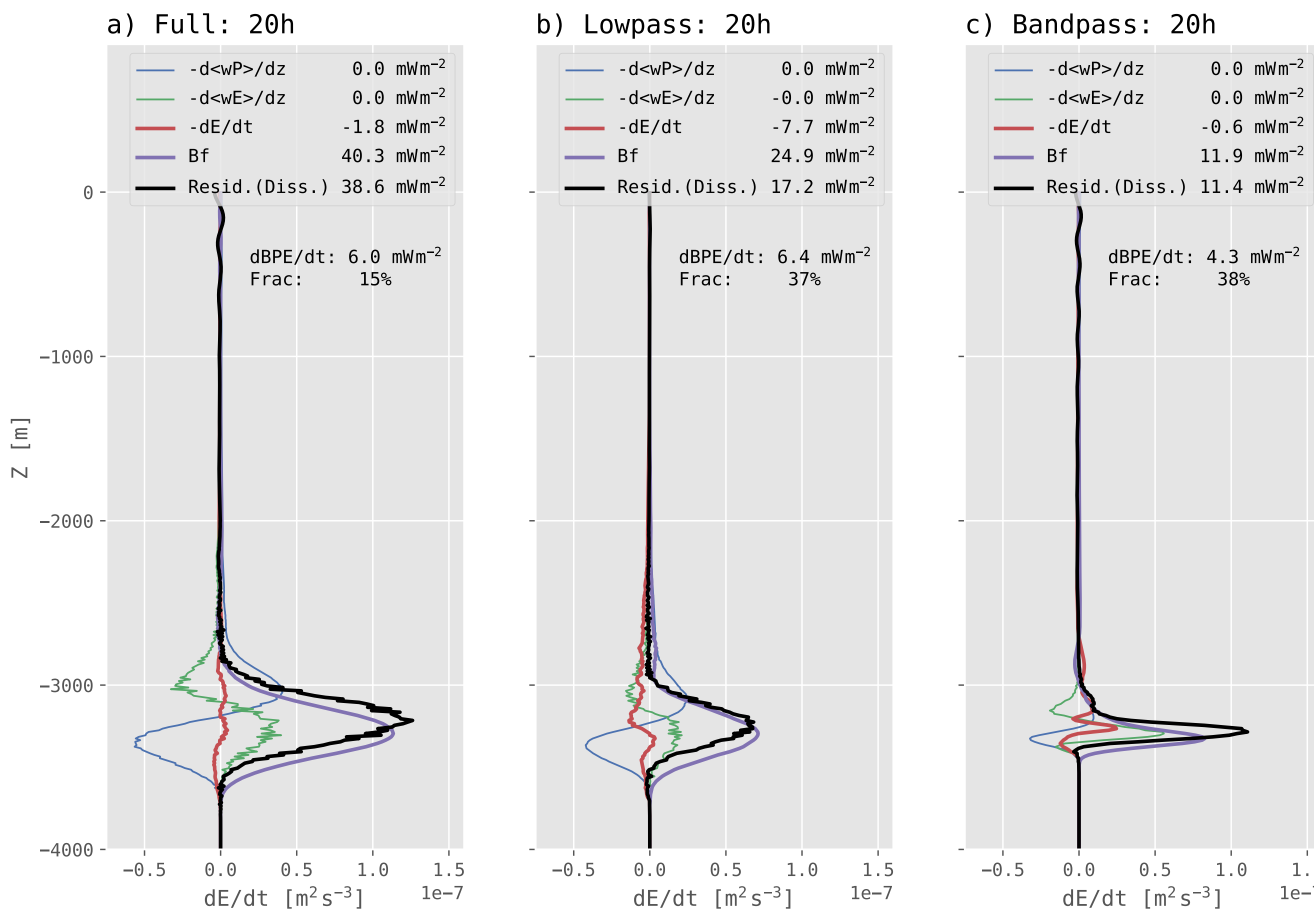

FIG. 6. Energy budget for a) FULL bathymetry, b) LOWPASS bathymetry and c) the BANDPASS bathymetry. Profiles are lateral integrals of the energy budget terms divided by the total domain area, not the area of the water at a given depth. The vertical integrals of the terms are indicated in the legend, again divided by the total domain area to get an average rate of energy change per area. The $dBPE/dt$ term is from changes in the background potential energy, and it is a fraction of the residual, as indicated. The residual is not always positive at all depths, reflecting modest inaccuracies in the energy budget.

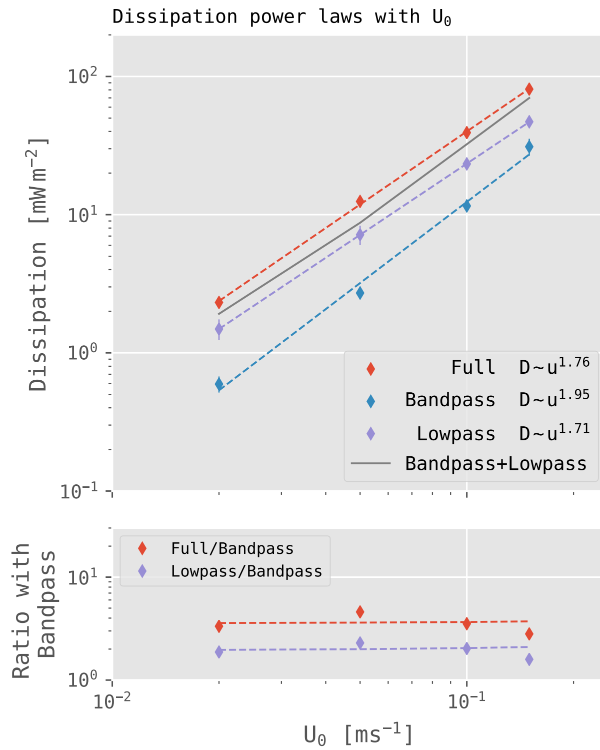

FIG. 7. Inferred dissipation for the BANDPASS, LOWPASS, and FULL topography simulations for four different forcing speeds, U_0. The power law versus the forcing is shown in the legend. The sum of the BANDPASS and LOWPASS dissipations is shown as the grey line. The bottom panel shows the ratio of the dissipation in the LOWPASS and FULL simulations to the BANDPASS simulations.

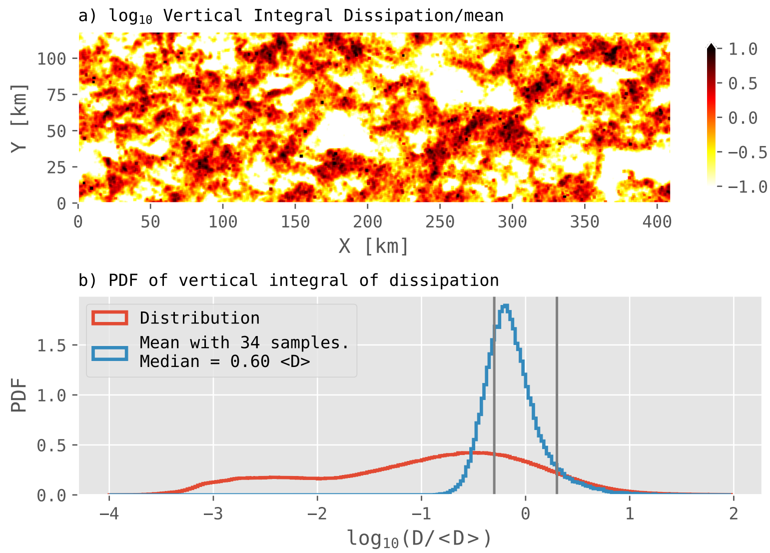

FIG. 8. a) Vertical integral of the turbulence dissipation returned by the turbulence scheme used in the FULL simulation. Note these dissipations are different than the energy residuals calculated above; however, the turbulence scheme should yield useful estimates of inhomogeneity of the dissipation. The results have been normalized by the mean dissipation over the figure. b) PDF of the vertical integral showing the very large tail of low dissipations (red). Grey vertical lines bracket estimates that are one half and twice the actual mean. The PDF of the results of a Monte Carlo computation of the mean using 34 random samples shows that random averages will tend to underestimate the dissipation with a median value of 0.6 the actual mean dissipation (blue curve), though some averages will overestimate if a hotspot is measured. 34 samples was chosen as the number of deep-sea casts collected during the DIMES experiment St. Laurent et al. (2012).

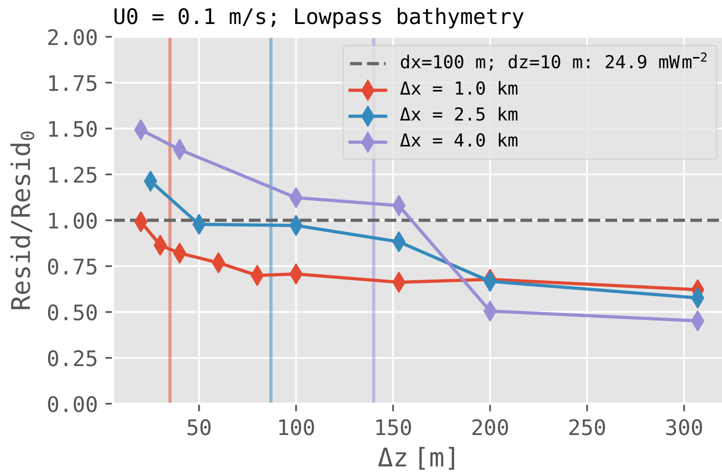

FIG. 9. Effect of changing lateral and vertical resolutions for the $U_0 = 0.1\ \mathrm{m\,s^{-1}}$ simulations over lowpass bathymetry. Three curves are for different lateral resolutions, as noted. Dashed line is the "true" lowpassed value for very high vertical and horizontal resolution. The vertical lines are the value of the vertical resolution of the simulation above which $\Delta z/\Delta x$ is greater than the root-mean-squared slope of the large-scale bathymetry ($\approx 2\pi/k_0$; equation (1)). When the slope is resolved then the simulations tend to over-predict the dissipation due to the large-scale bathymetry, and under-predict when the vertical resolution is too coarse.